T-matrix computations of light scattering by red blood cells

Nilsson, Annika M. K.; Alsholm, Peter; Karlsson, Anders; Andersson-Engels, Stefan

1998

CODEN:LUTEDX/(TEAT-7068)/1-24/(1998)

T-matrix computations of light scattering by red blood cells

Annika M. K. Nilsson, Peter Alsholm, Anders Karlsson, and Stefan Andersson-Engels

Department of Electroscience
Electromagnetic Theory
Lund Institute of Technology
Sweden

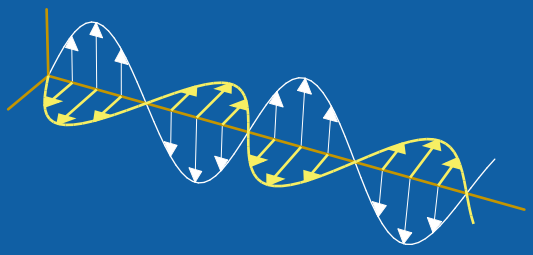

Annika M. K. Nilsson, Peter Alsholm, and Stefan Andersson-Engels

Department of Physics
Lund Institute of Technology
P.O. Box 118
SE-221 00 Lund
Sweden

Anders Karlsson

Department of Electroscience
Electromagnetic Theory
Lund Institute of Technology
P.O. Box 118
SE-221 00 Lund
Sweden

Editor: Gerhard Kristensson

Abstract

The electromagnetic far field, as well as near field, originating from light interaction with a red blood cell (RBC) volume equivalent spheroid, were analyzed utilizing T-matrix theory. This method is a powerful tool which enables the influence of cell shape on the angular distribution of scattered light to be studied. General observations were that the three-dimensional shape, as well as optical thickness apparent to the incident field, affect the forward scattering. The back scattering was influenced by the shape of the surface facing the incident beam. Furthermore, sphering as well as elongation of an oblate shaped RBC into a volume equivalent sphere or prolate shaped spheroid, respectively, were theoretically modeled in order to imitate physiological phenomena caused, e.g., by sphering agents, heat or increased shear stress of flowing blood. Both sphering and elongation were shown to decrease the intensity of the forward directed scattering, thus yielding lower g-factors. The sphering made the scattering pattern independent of the azimuthal scattering angle ϕ_s, while the elongation induced more apparent ϕ_s-dependent patterns. The light scattering by an RBC volume equivalent spheroid, was thus found to be highly influenced by the shape of the scattering object. A near-field radius, rnf, was evaluated as the distance to which the maximum intensity of the total near field had decreased to 2.5 times that of the incident field. It was estimated to 2-24.5 times the maximum radius of the scattering spheroid, corresponding to 12-69 μm. When the absorption properties of a red blood cell were incorporated in the computations, the near-field radius was only slightly reduced by 0.2-0.6 times the maximum radius. As the near-field radius was shown to be larger than a simple estimation of the distance between the RBCs in whole blood, the assumption of independent scattering, frequently employed in optical measurements on whole blood, seems inappropriate. This also indicates that results obtained from diluted blood, cannot be extrapolated to whole blood, by multiplying with a simple concentration factor.

1 Introduction

Optical measurements on blood both in vivo and in vitro seems to be an ever growing field, since clinically useful information, expressed in terms of fundamental haematological parameters, can be extracted with rather simple and non-destructive measurement procedures. Traditionally, these measurements are focused on the optical absorption properties of blood. Despite its general character, the macroscopic average absorption parameter reveals several relevant, physiological properties of blood, such as the degree of oxygen saturation, concentration of haemoglobin and other light absorbing solutes that are characteristic of blood and thus relevant to the state of the patient's health. Measurements of optical absorption properties of blood are often performed by recording either reflected, [5, 20, 28, 30] or transmitted [6, 13, 32] probing light from, or through a blood sample, or blood perfused tissue. A theoretical multiple scattering model, for example the diffusion approximation of the transport equation [28, 30], inverse adding-doubling computations (IAD) [26]

or Monte Carlo simulations [8], is then applied in order to relate the measured quantities (transmittance and/or reflectance) to the optical absorption parameter of blood.

However, there is a growing interest in the scattering properties of blood, partly since a correct compensation for light scattering improves the accuracy of the absorption measurements, but mainly as the scattering properties themselves provide interesting information on morphological properties of the blood cells [4, 14, 15, 25, 26, 32, 35]. Equivalent with the absorption properties of blood, the macroscopic average scattering properties can be determined by applying the previously mentioned theoretical multiple scattering models. However, the macroscopic scattering parameters do not yield detailed morphological information on the blood cells. To be able to extract microscopic information, such as cell size, shape and alignment, a detailed and explicit model is needed; one which treats the light scattering from each individual cell. Several such methods are available, all based on the solution of Maxwell's equations for an object with a shape similar to that of the cell, but each applying different approximations required to obtain the angular distribution of the scattered light [11, 36]. The choice of model is based on the properties of the object being modeled, since this governs which approximations are realistic and valid. A red blood cell (RBC) has a size in the order of 10 times larger than the wavelength in the optical region, which means that neither Rayleigh scattering, consisting of an approximation valid for small scatterers compared to the wavelength, nor geometrical optics theory for large scatterers can successfully be applied. Instead, other approximate models such as Fraunhofer diffraction, Anomalous diffraction and Rayleigh-Gans-Debye scattering have been applied for red blood cells [21, 33], as well as the exact solution of Maxwell's equations for a homogeneous or layered sphere, i.e. the Lorentz-Mie theory [16–18, 21, 31]. The latter method, has been applied to evaluate the influence of the size of randomly oriented RBCs on the optical scattering properties, by performing Mie calculations for spheres with different RBC equivalent size [31] and comparing the theoretically obtained scattering properties with those measured. The successful results of that study indicate that size rather than shape affects the light scattering from a suspension with randomly oriented cells. However, random orientation of RBCs is experimentally seldom realistic, as optical measurements often are performed on blood in motion. A certain preferred alignment of the disc-shaped cells is introduced and the asymmetric shape of the cells has been shown to influence the angular distribution of scattered light [4]. Parameters such as direction and degree of alignment of the cells versus the direction of the incident beam, as well as cell shape are essential in the evaluation of optical measurements on flowing blood. In order to study the influence of cell shape on scattered light, we have employed the so called T-matrix formalism [3, 38]. It is a scattering method that solves Maxwell's equations for e.g. oblate- and prolate spheroids using expansions in global spherical vector waves. Computations have previously been performed on spheroidal particles with a size in the same range as the wavelength, such as soil particles [10], aerosols [22] and hematite particles [29]. Numerically it is found that the precision of the real and complex numbers, used in the computations, has to increase when the size of the studied particle increases,

in order to obtain accurate results. Thus, convergent solutions are not found for particles with large size parameters or pronounced asymmetric shapes, such as for RBC volume equivalent spheroids, when utilizing normal precision variables (8-digit numbers) in the computations. Mishchenko and Travis [24] opened up the door to T-matrix computations of light scattering by larger spheroids by demonstrating that convergence is improved when using extended precision (32-digit numbers). Hence, extended precision variables are used in this study. To the best of our knowledge this is the first theoretical study of light scattering by RBCs employing the T-matrix formalism. We would thus like to introduce this powerful method in the field of tissue optics. Utilizing this numerical method, we have studied the changes in the angular distribution of both the far- and near field of scattered light from an RBC, induced by the alignment of the cells and two realistic shape transformations, i.e. sphering and elongation.

2 T-matrix formalism

The general idea of the T-matrix theory is to expand the incident and surface electric fields, $\boldsymbol{E}_{\mathrm{i}}$ and $\boldsymbol{E}_{\mathrm{surf}}$, as well as the internal and scattered fields, $\boldsymbol{E}_{\mathrm{int}}$ and $\boldsymbol{E}_{\mathrm{s}}$, in terms of appropriate sets of vector waves. By utilizing integral representations of the fields, a relation between the expansion coefficients for the incident and scattered fields is obtained.

The electric fields, with a wavelength in the medium of λ, should satisfy the Maxwell equations, rephrased in the vector Helmholtz equation, i.e.

$$\nabla \times \nabla \times \boldsymbol{E} - k^2 \boldsymbol{E} = 0 \tag{2.1}$$

where $k = 2\pi/\lambda$ is the wavenumber. For a spheroidal scattering object, the appropriate basis functions are spherical vector waves, $\boldsymbol{M}_\nu$ and $\boldsymbol{N}_\nu$, with ν representing the spherical harmonic double index m and n. When the time dependence $e^{-i\omega t}$ is used ($\omega = 2\pi c/\lambda$, where c is the speed of light), these functions are given by

$$\begin{aligned} \boldsymbol{M}^o_\nu(\boldsymbol{r}) &== \nabla \times \boldsymbol{r} e^{-im\phi} P^m_n(cos\theta)\,(j_n(kr) + in_n(kr)) \\ \boldsymbol{N}^\circ_\nu(\boldsymbol{r}) &= k^{-1} \nabla \times \boldsymbol{M}_\nu(\boldsymbol{r}) \end{aligned} \tag{2.2}$$

with geometric parameters defined in Figure 1 a). Here $P^m_n(cos\theta)$ are the associated Legendre functions, $j_n(kr)$ are the spherical Bessel functions, $n_n(kr)$ the Neumann functions and the indices are n =0, 1, 2..., $m = -n, -n+1, \ldots, n-1, n$. These functions are outward traveling waves that are singular at the origin. They satisfy the Helmholtz vector equation and form a complete set of functions on the unit sphere. The corresponding functions that are regular at the origin are obtained by excluding the Neumann function, $n_n(kr)$, in Eq. (2.2). Thus, the regular vector waves, $\boldsymbol{M}^r_\nu(\boldsymbol{r})$ and $\boldsymbol{N}^r_\nu(\boldsymbol{r})$, have a pure Bessel function radial dependence. The incident field in the surrounding medium is regular at the origin and is thus expanded in regular waves:

$$\boldsymbol{E}_i(k_{\mathrm{surmed}}\boldsymbol{r}) = E_0 \sum_\nu D_\nu \left(a_\nu \boldsymbol{M}^r_\nu(k_{\mathrm{surmed}}\boldsymbol{r}) + b_\nu \boldsymbol{N}^r_\nu(k_{\mathrm{surmed}}\boldsymbol{r})\right) \tag{2.3}$$

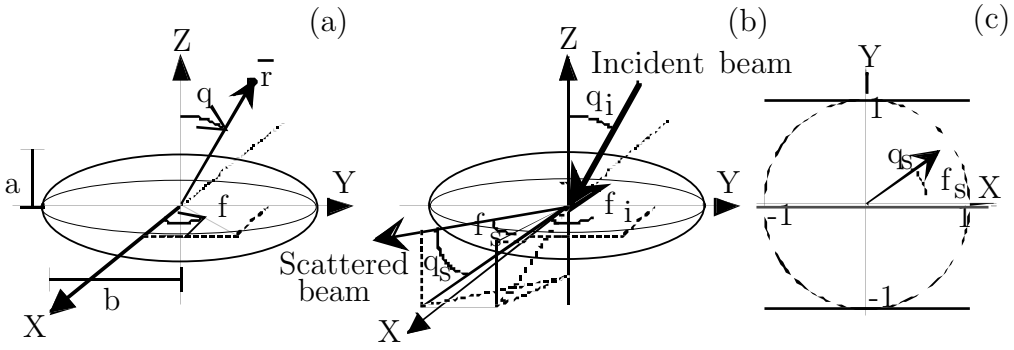

Figure 1: The reference systems used are shown in (a) for the derivation of the T-matrix formalism, in (b) to describe the geometry of the incident and scattered light in conjunction with T-matrix computations and in (c) when presenting the results of the T-matrix computations as the intensity of scattered light on a planar grid.

E_0 is the amplitude of the incident field, D_ν is a normalization constant and finally a_ν and b_ν are the expansion coefficients. The coefficients a_n and b_n are assumed to be known and are, for an incident plane wave, expressed in terms of associated Legendre functions and their derivatives [38]. The internal field within the object is expanded in the same regular vector waves:

$$\boldsymbol{E}_{\text{int}}(k_{\text{object}}\boldsymbol{r}) = E_0 \sum_{\mu} \left(c_\mu \boldsymbol{M}^r_\mu(k_{\text{object}}\boldsymbol{r}) + d_\mu \boldsymbol{N}^r_\mu(k_{\text{object}}\boldsymbol{r}) \right) \tag{2.4}$$

where μ incorporates the two spherical harmonics indices mentioned earlier and c_μ and d_μ are the expansion coefficients of the internal field. Finally, the scattered field is outgoing and is expanded in outgoing spherical waves, i.e. by keeping the Neumann function in Eq. (2.2):

$$\boldsymbol{E}_s(k_{\text{surmed}}\boldsymbol{r}) = E_0 \sum_{\nu} D_\nu \left(f_\nu \boldsymbol{M}^0_\nu(k_{\text{surmed}}\boldsymbol{r}) + g_\nu \boldsymbol{N}^0_\nu(k_{\text{surmed}}\boldsymbol{r}) \right) \tag{2.5}$$

where f_n and g_n are the expansion coefficients characterizing the scattered field. They, and thus the expression describing the angular distribution of the scattered light, Eq. 2.5, are obtained by multiplying the known expansion coefficients of the internal field by a so called transition matrix, or T-matrix:

$$\begin{pmatrix} f_\nu \\ g_\nu \end{pmatrix} = - \begin{pmatrix} \text{T-} \\ \text{matrix} \end{pmatrix} \begin{pmatrix} a_\nu \\ b_\nu \end{pmatrix} \tag{2.6}$$

The problem is thus reduced to computations of the expansion coefficients of the incident field and of the elements of the T-matrix. The derivation of the elements of the T-matrix is extensively described by [38] as well as by Barber and Yeh [3]. Briefly, the internal field, resulting from the incident field, can be thought of as inducing polarization currents within the spheroid, which in turn produces the scattered

field. Thus, the connection between the scattered and incident field, mathematically expressed by the T-matrix, lies physically in the internal field. In order to simplify the mathematical analysis, the internal polarization currents are replaced by an equivalent distribution of electric and magnetic currents on the surface of the object. These currents are related to and can be derived from the known incident field, as their resultant field inside the spheroid should cancel the incident field, forming a null field within the scattering object, according to the so called equivalence theorem [3, 38]. The surface currents are also related to the scattered field as they are the source of the external, scattered light. The scattered field is obtained by computing surface integrals with the surface currents as the integrands. Thus, the scattered field is via surface integrals related to the surface currents, which in turn are related to the incident field via the equivalence theorem. This means that the expansion coefficients of the scattered field are related to those of the internal field, which can be expressed in matrix form as follows:

$$\begin{pmatrix} f_\nu \\ g_\nu \end{pmatrix} = -i \begin{pmatrix} \text{B-} \\ \text{matrix} \end{pmatrix} \begin{pmatrix} c_\mu \\ d_\mu \end{pmatrix} \tag{2.7}$$

The elements of the B-matrix are composed of surface integrals of the surface currents. Furthermore, the expansion coefficients of the internal field are related to those of the incident field, applying the equivalence theorem:

$$\begin{pmatrix} \text{A-} \\ \text{matrix} \end{pmatrix} \begin{pmatrix} c_\mu \\ d_\mu \end{pmatrix} = -i \begin{pmatrix} a_\nu \\ b_\nu \end{pmatrix} \tag{2.8}$$

Also the elements of the A-matrix are composed of surface integrals. The T-matrix handles and combines these two steps by relating the expansion coefficients of the incident field directly to those of the scattered field:

$$\begin{pmatrix} f_\nu \\ g_\nu \end{pmatrix} = - \begin{pmatrix} \text{B-} \\ \text{matrix} \end{pmatrix} \begin{pmatrix} \text{A-} \\ \text{matrix} \end{pmatrix}^{-1} \begin{pmatrix} a_\nu \\ b_\nu \end{pmatrix} = - \begin{pmatrix} \text{T-} \\ \text{matrix} \end{pmatrix} \begin{pmatrix} a_\nu \\ b_\nu \end{pmatrix} \tag{2.9}$$

The elements of the T-matrix are composed of computationally tolerable surface integrals. Moreover, when the scattering object is axi-symmetric, as for the spheroid, the surface integrals can be reduced to one dimensional line integrals, simplifying the computations further. In the case of spherical objects, the T-matrix is diagonal and the matrix elements can be computed analytically. The explicit expression of the scattered field is then identical to that obtained by Lorentz-Mie theory.

3 Computations

The T-matrix is determined by the wave numbers k_{surmed} and k_{object}, as well as by the geometry of the object, but is independent of the incident field. In this study, the

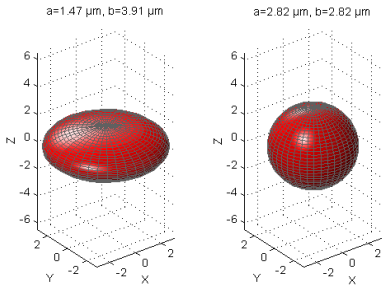

Figure 2: The geometrical shape and input parameters of the RBC volume equivalent spheroids used for the T-matrix computations are illustrated. The volume equivalent oblate spheroid (axial ratio: 0.375, size parameter: 19.6) and the sphere (axial ratio:1, size parameter: 37.7) are shown here and the three prolate spheroids (I-III) with different elongations in Figure 3 below. Computations were performed at the wavelength 632.8 nm, as well as at 940 nm for the two particles here with the corresponding size parameters 13.2 for the oblate spheroid and 25.4 for the sphere.

scattering particles are spheroidal with half axes a and b, as depicted for an oblate spheroid in Figure 1 a). Further parameters used to characterize the spheroid are the size parameter, $x = 2\pi a/\lambda$, with the wavelength λ compensated for the refractive index of the surrounding medium, the axial or aspect ratio a/b, and finally the real (m_r) and imaginary part (m_i) of the relative refractive index:

$$m_r + im_i = n_{\text{object}}/n_{\text{surmed}} \tag{3.1}$$

The T-matrix formalism described above provides an exact solution to the problem of light scattering by axi-symmetric objects, under the condition that the fields in Eqs. (2.3)-(2.5) are all expanded in infinitely many elements. This results in a T-matrix of infinite size and in conjunction with practical computations the expansion series must be truncated. It follows from this that the convergence of the computations has to be considered, in order to reach a correct solution within the required accuracy. Three convergence parameters are often employed; the number of integration points needed in the line integrals of the elements in the T-matrix for accurate numerical integration, and the maximum values of the indices m and n in the truncated series of Eq. (2.3). A convergence check is of particular importance, since T-matrix computations for large objects require very accurate calculations of the matrix elements, as well as large matrices. Initial small numerical errors can otherwise result in manifest errors in the final T-matrix. Applying single precision variables in a widely used T-matrix computer program [2] yields good accuracy for small (compared to the wavelength) and weakly aspherical spheroids with size parameters $x < 25$ and axial ratios close to unity. T-matrix computations of spheroidal particles with a similar shape and volume as the large (compared to the wavelength), highly aspherical red blood cell have thus previously not been possible. Mishchenko and Travis [24] have shown that high enough accuracy can be achieved for 2-2.7 times higher size parameters, by employing extended precision (32-digit numbers).

We have therefore expanded the range of size parameters, within which the

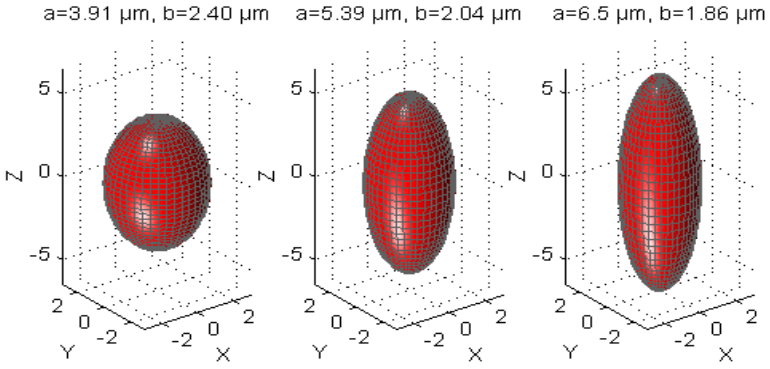

Figure 3: The geometrical shape and input parameters of the three prolate spheroids (Prolate I to the left with an axial ratio of 1.63 and size parameter of 35.2, Prolate II/III with the corresponding parameters 2.64/3.5 and 48.4/58.4, respectively) with different elongations used for the T-matrix computations are illustrated. Computations were performed at the wavelength 940 nm.

program of Barber and Hill [2] converges, by incorporating extended precision of the variables used. However, as extended precision was not easily incorporated in both real and imaginary parts of the complex variables, we focused on the real part.

This excluded the option of modeling the consequence of light absorption within the scattering spheroid and its impact on the scattered field, as light absorption is expressed by an imaginary refractive index. To be able to estimate the significance of the influence of light absorption, a program with double precision variables (16-digit numbers) was developed, enabling the complex refractive indices to be included. It provided us with the means to compare results from computations, with and without absorption, for spheroids with size parameters similar to those used in the extended precision program, but with axial ratios closer to unity. Once the T-matrix was computed, either a far-field or a near-field program (both modified with extended and double precision variables) was employed in order to compute the resulting scattered far- or near field. The far field is the scattered field found at rather large distances from the scattering object, i.e. when $r > \lambda$ and $r > 2b$ and $r > (2b)^2/\lambda$, resulting in a field with a radial dependence of e^{ikr}/r. In regions closer to the object, this far-field approximation is not valid. We refer to the field in this region as the near field. Extensive comparisons between results obtained from the original and the modified programs were conducted. All comparisons showed good correspondence, confirming the accuracy of the modified code.

3.1 The far field

The angular scattering distributions were computed for the far field employing the extended precision T-matrix programs for five RBC volume equivalent homogeneous

spheroids, shown in Figures 2 and 3. The volume of a red blood cell [7] was taken to be 94 μm^3, the refractive index of the surrounding blood plasma as 1.34514, and the real part of the relative refractive index as 1.045 [7], neglecting the absorption ($m_i = 0$). Assuming wavelengths of 632.8 nm and 940 nm, a normal RBC was modeled as a volume equivalent oblate with corresponding size parameters of 19.6 and 13.2, respectively, and an axial ratio of 0.375, shown to the left in Figure 2. The azimuthal angle of the incident light, ϕ_i in Figure 1 b), was selected as 0°, since it does not affect the results due to the symmetry of the spheroids. Computations were performed for $\theta^i = 0°$, 45° and 90° (see Figure 1 b) with both parallel and perpendicular (to the xz plane) polarization of the incident plane wave. The influence of sphering was modeled by computing the light scattering, at the same wavelengths, by an RBC volume equivalent sphere with parameters shown to the right in Figure 2). Computations were performed for $\phi_i = \theta_i = 0°$, as neither of the incident angles affect the results due to complete symmetry of the sphere. The angular distribution of the scattered light was again obtained for both parallel and perpendicular polarization of the incident plane wave. Finally, the influence of elongation of the RBC was studied by computing the light scattering at the wavelength 940 nm by a volume equivalent prolate spheroid, by varying the axial ratio from 1.63 to 3.5 as depicted in Figure 3) (Prolate I-III). The incident angles here were $\phi_i = 0°$ and $\theta_i = 90°$ and computations were performed for both polarization directions. The logarithm of the intensity of the scattered light is presented in relative units in planar grids with the zenith scattering angle (s mapped along the radius r_{pg} ($\theta_s = 0°$ when $r_{pg} = 0$ and $\theta_s = 180°$ when $r_{pg} = 1$) and the azimuthal scattering angle ϕ_s mapped in the normal way according to cylindrical coordinates (see Figure 1 b) and c)). Values outside the unit circle are set to the logarithm of the back-scattered intensity. To be able to interrelate the angular distributions of the scattered light of differently shaped cells, the scattering probability was computed as a function of the zenith scattering angle θ_s. This scattering probability, $P_{diff}(\theta_s, \phi_s)$, was calculated by numerical integration of the differential scattering probability, $P_{diff}(\theta_s, \phi_s)$, over all azimuthal angles $\phi_s = 0 - 2\pi$:

$$P_{\theta_s} = \int_0^{2\pi} P_{diff} \sin\theta_s d\phi \tag{3.2}$$

where

$$\int_0^{2\pi} \int_0^{\pi} P_{diff} \sin\theta d\theta d\phi = 1 \tag{3.3}$$

The differential scattering probability, $P_{diff}(\theta_s, \phi_s)$, was defined as the ratio of the differential scattering cross section, $\sigma_{\text{diff}}(\theta_s, \phi_s)$ (proportional to the intensity of the scattered light in the direction θ_s and ϕ_s shown in Figures 4 and 5) to the total scattering cross section σ_{tot} (derived as the differential scattering cross section integrated over the entire unit sphere) [2]. Furthermore, the angular distribution of

the scattering probability was quantified by one single parameter, i.e. the average of the cosine of the deflection angle:

$$g =< \cos\theta_s > \tag{3.4}$$

3.2 The near field

Independent scattering of a collection of spheroids can be assumed when the distance between the particles is large enough for the near fields to decline. We have therefore studied the extension of the near field of a single spheroid in order to estimate the inter-particle distance required to be able to neglect the influence of surrounding scattering particles. The near field was computed for the same spheroids as those treated in the far-field section, as shown in Figure 2, employing the near-field computer program with extended precision variables. The incident plane wave propagates in the positive x-direction direction with the polarization direction specified as either parallel or perpendicular to the xy plane. The results are presented as intensity in relative units versus x and y coordinates in the equatorial plane of the spheroid. A near-field radius, r_{nf}, was here defined as the distance from the center of the particle, to where the maximum intensity of the total field had decreased to 2.5 times that of the incident field. The near-field radius was expressed in terms of the maximum radius of the spheroid, r_{csc} (the radius of a circumscribed circle). If the maximum intensity never exceeds the limit value of 2.5 times the incident field then rnf was set to r_{csc}. The near-field radius was evaluated for all computed near fields.

The influence of absorption on the near-field was estimated by employing the imaginary part of the refractive index of the spheroid in the near-field program with double precision variables. Computations were performed for spheroids with size parameters similar to those used previously for extended precision computations (Figure 2), but with less asymmetric shape in order to obtain convergence of the solutions employing double precision variables. Scattering objects were here prolate spheroids with size parameters in the range 27.0-40.5 and axial ratios between 1.10 and 2.02, as well as oblate spheroids with size parameters between 16.5 and 22.4 and axial ratios in the range 0.523-0.831. Two computations were performed for each spheroid; one with the imaginary relative refractive index, m_i, set to zero (no absorption) and one with $m_i = 0.000113$, which is a characteristic value for red blood cells [28]. The near-field radius was then evaluated and compared for the two corresponding computations with absorbing and non-absorbing spheroids.

4 Results

4.1 The far field

The angular far-field distributions of scattered light, computed at the wavelength 632.8 nm for the RBC volume equivalent sphere and oblate (depicted in Figure 2) are mapped onto planar grids in logarithmic scale in Figure 4. Only the results

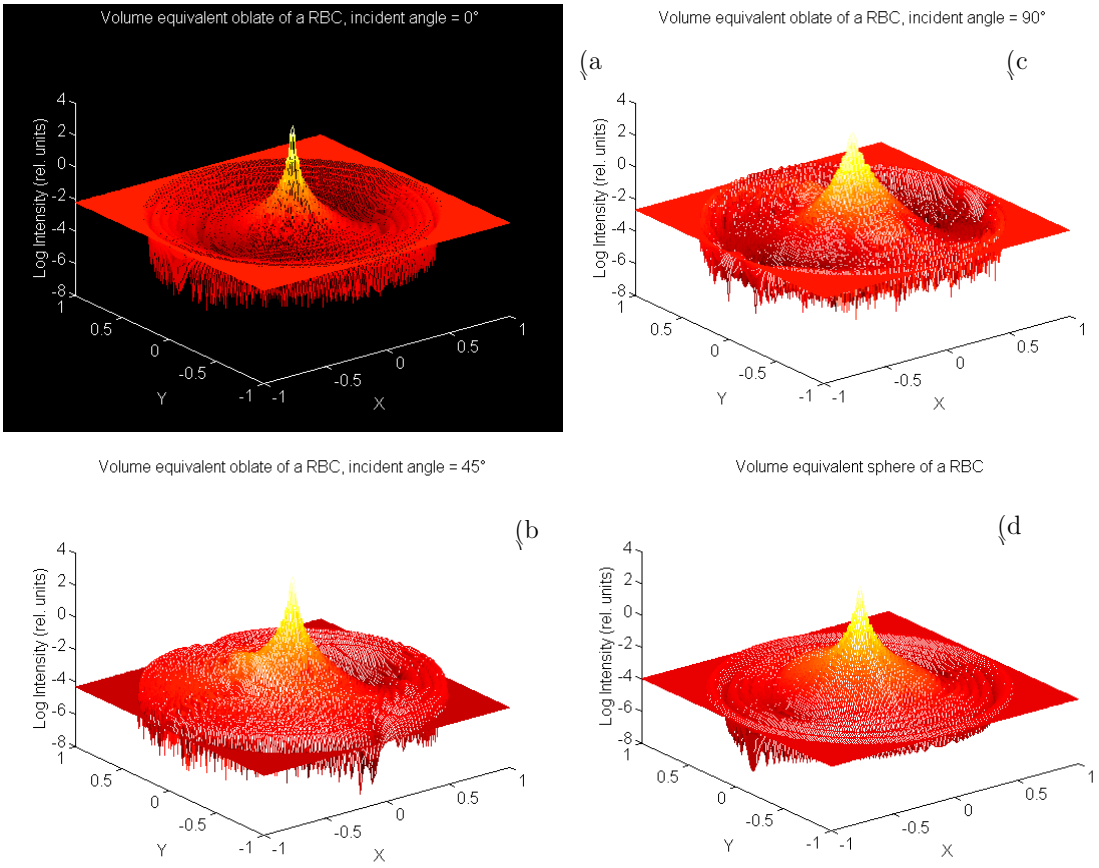

Figure 4: Planar grids of the angular distribution of the scattered light resulting from T-matrix computations employing parallel polarization of the incident plane wave with a wavelength of 632.8 nm are presented. The intensity is shown on a logarithmic scale (base 10) and arbitrary units versus the azimuthal scattering angle ϕ_s and the zenith scattering angle θ_s, mapped onto the normal azimuthal angle and the radius in the planar grid, respectively. The scattering pattern originating from the RBC volume equivalent oblate spheroid with $\theta_i = 0°$ is shown in (a) with a value of 3.25 (relative units) for the log intensity of the forward scattering ($\phi_s = \theta_s = 0°$) and -2.18 for the log intensity of the back scattering ($\theta_s = 180°$). Corresponding planar grids are shown in (b) $\theta_s = 180°$ with a log intensity of the forward and back scattering of 3.19 and -4.29 and in (c) $\theta_i = 90°$ with the values 2.83 and -2.64, respectively. The distribution of the scattered light from the RBC volume equivalent sphere is shown in (d) with a log intensity of the forward and back scattering of 2.48 and -3.95.

of parallel (to the xz plane) polarized incident light are shown, since the direction of polarization was found to have a minor influence on the results. The scattered light by the RBC volume equivalent oblate was analyzed for $\theta_i = 0°$, 45° and 90°. Common to all graphs is the circular ripple structure. From an experimental point of view these ripples are of minor interest, since they are averaged out when analyzing and measuring light scattered by an assembly of spheroids, which do not have exactly the same size and orientation. Comparing the three graphs from the oblate spheroid in Figures 4 a-c, we note that the peak of forward scattering is decreased and broadened with higher incident angles. It is also clear that the θ_s-dependence is in general much stronger than the ϕ_s-dependence. When the light is incident along the symmetry axis (the z-axis) of the oblate spheroid ($\phi_s = \theta_i = 0°$), the angular distribution of scattered light is more or less independent of the azimuthal angle ϕ_s with merely a weak, wavy pattern at $\phi_s = 0°$ and 180° ($Y = 0$). However, characteristic ϕ_s-dependent patterns appear in the distribution of scattered light for larger incident angles at $\theta_i = 45°$ and 90°. Local minima and maxima are obtained depending on the shape of the surface of the spheroid the incident light faces. The back-scattered light, mapped on the unit circle of the planar grids, seems to be highly dependent on the curvature facing the incident light. When the incident light faces any of the stagnation points of the surface of the spheroid ($\theta_i = 0°$ and 90°), localized where the equatorial plane and the symmetry axis cross the surface, the back scattering is significantly higher than for the case of obliquely incident light (e.g. $\theta_i = 45°$). The light distribution in Figure 4 d) is completely symmetric versus the azimuthal angle ϕ_s, in accordance with the symmetric shape of the sphere. It shows a smooth decline with increasing zenith deflection angle θ_s mapped along the radial axis in the planar grid. It is also evident that the forward scattering peak, originating from the sphere, is lower and broader than those of the oblate spheroid at zenith incident angles of 0° and 45°. A lower forward scattering peak can also be observed for the oblate spheroid at an incident angle of 90°, compared to that of the sphere. However, there is no clear difference in the width of the peak and the back scattering is significantly higher for the oblate spheroid than that of the sphere. Figure 5 shows the planar grids of the scattered light intensity on a logarithmic scale, obtained at a wavelength of 940 nm from the RBC equivalent prolate spheroids depicted in Figure 3). The incident angles are $\phi_i = 0°$ and $\theta_i = 90°$. Since the incident angle θ_i is perpendicular to the symmetry axis, a rather strong ϕ_s-dependency is seen for all prolate spheroids in Figures 5 a-c. These can be seen as dips at approximately $\phi_s = 0°$ and 180° ($Y = 0$) at intermediate zenith scattering angles θ_s. The dips become deeper with a more pronounced elongation of the spheroid. The forward scattering peak is also influenced by the elongation and shows a significant decrease in height with increasing elongation in these three cases. This is in contrast to the back scattered light, which displays an increase with the elongation.

The angular distributions of the scattered light, obtained from different spheroids and incident angles, are interrelated in two-dimensional plots of the scattering probability versus the zenith scattering angle θ_s. Figure 6 presents the scattering probability for light with a wavelength of 632.8 nm, scattered by the oblate spheroid

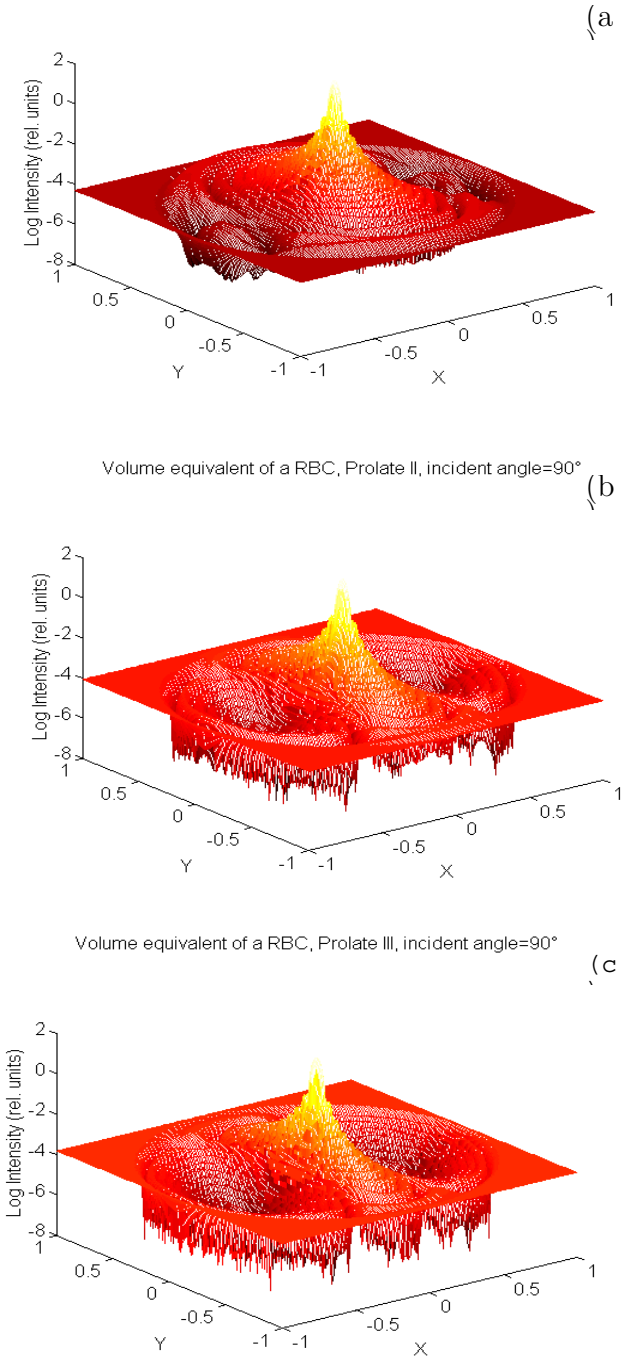

Figure 5: Planar grids of the angular distribution of the scattered light resulting from T-matrix computations of prolate spheroids, employing parallel polarization of the incident light with a zenith incident angle of 90° and a wavelength of 940 nm are presented. The intensity is presented on a logarithmic scale (base 10) and arbitrary units. The results of Prolate I are shown in (a) with a log intensity of the forward and back scattering of 1.72 and 4.31 (relative units), of Prolate II in (b) with corresponding values of 1.46 and -4.05 and finally of Prolate III in (c) with a log intensity of the forward and back scattering of 1.31 and -3.81.

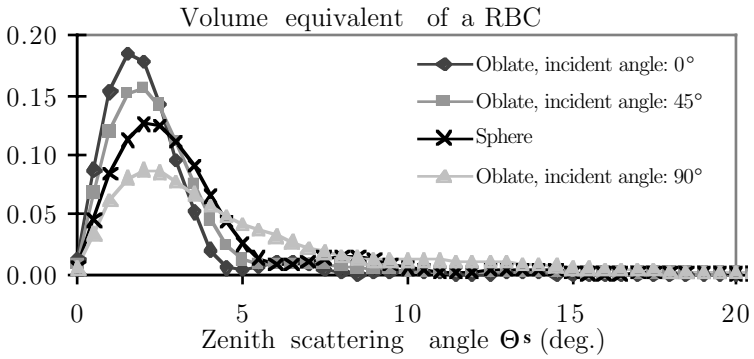

Figure 6: The scattering probability is plotted versus the zenith scattering angle for the oblate spheroid with the incident angles $\theta_i = 0°$, 45° and 90° at the wavelength 632.8 nm (grey lines). The black line represents the scattering probability of the volume equivalent sphere.

and the sphere. Despite the large intensity at small deflection angles in Figure 4, the scattering probability is seen to be much smaller at deflection angles in the region $0° - 2°$ in Figure 6 than in the region $2° - 3°$. This originates from the fact that the scattering probability, P_{θ_s}, is proportional to $\sin\theta_s$ times the differential scattering probability (proportional to the intensity) integrated over $0 < \phi \leq 2\pi$, due to the surface element $\sin\theta d\theta d\phi$ of the unit sphere (see Eqs. 11 and 12). From Figure 6 it is evident that the forward scattering peak is higher and more narrow for the oblate spheroid at zenith incident angles of 0° and 45° than for the sphere, while an incident angle of 90° yields a lower and broader forward scattering than that of the sphere, as already indicated in the planar grids. Thus, the incidence of light closer to the symmetry axis (small θ_i) yields higher and more narrow peaks in the forward direction, than with zenith incident angles θ_i close to 90°. The latter phenomenon can also be seen for an RBC volume equivalent oblate at the wavelength 940 nm, as represented by the grey curves in Figure 7. In addition, a slight shift in the maximum scattering probability to larger deflection angles with larger incident angles θ_i can be observed for the oblate spheroid in both Figures 6 and 7. Figure 7 also includes scattering probability curves at a wavelength of 940 nm for RBC volume equivalent prolate spheroids (Prolate I-III depicted in Figure 3 with increasing elongation. A decrease in the scattering probability in the forward direction is shown for these three cases, as well as a slight shift of the maximum value to smaller zenith scattering angles θ_s with increasing elongation.

Further analysis of the angular distribution of the scattering probability was performed by associating a g-factor to each curve. The results were obtained for incident angles of $\theta_i = 0°$, 45° and 90° from the symmetry axis and the three individually extracted g-factors for each spheroid were averaged to form a simple approximation of randomly oriented particles. The results are listed in rows in Table 1, starting with g-factors obtained from light impinging on the particle along the major axis and ending with incidence along the minor axis. From this it follows that the incident angle versus the symmetry axis, θ_i, is listed in the opposite order for the oblate

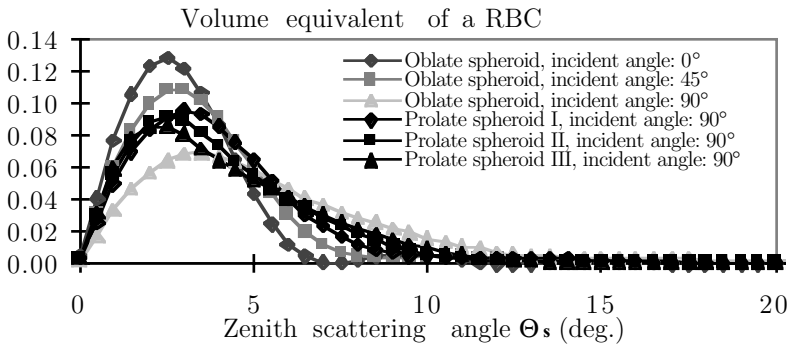

Figure 7: The scattering probability is plotted versus the zenith scattering angle for the oblate spheroid with the incident angles $\theta_i = 0°$, 45° and 90° at the wavelength 940 nm (grey lines). The black lines correspond to results obtained for the volume equivalent prolate spheroids I-III with an incident angle of 90° and the same wavelength.

Incident angle vs. major axis	Oblate 632.8 nm	Sphere 632.8 nm	Oblate 940 nm	Sphere 940 nm	Prolate I 940 nm	Prolate II 940 nm	Prolate III 940 nm
0°	0.989	0.993	0.989	0.992	0.989	0.986	0.985
45°	0.996	0.993	0.993	0.992	0.991	0.990	0.990
90°	0.997	0.993	0.994	0.992	0.992	0.991	0.990
Average	0.994	0.993	0.993	0.992	0.991	0.989	0.988

Table 1: The influence of particle shape and incident angle on the g-factor. Note that the incident angle is given versus the major axis. It is equivalent with the symmetry axis for the prolate but perpendicular to that of the oblate spheroid.

as compared to the prolate spheroid. From Table 1 it is thus clear that the g-factor increases when the direction of the incident light approaches the minor axis of the spheroid. Furthermore, a decrease in the g-factor is seen at incident angles of 45° and 90° versus the major axis for both wavelengths evaluated (632.8 and 940 nm), when an oblate spheroid turns spherical without changing the volume. However, the very opposite, i.e. a slight increase, is observed for both wavelengths at an incident angle of 0° versus the major axis. Still, the average values of the RBC volume equivalent oblate spheroid and sphere show a slightly smaller g-factor for the sphere than for the oblate spheroid.

4.2 The near field

The total near field was computed at the wavelengths 632.8 nm and 940 nm and the results obtained at 940 nm are for all RBC volume equivalent particles mapped onto the equatorial plane of the particles shown in Figures 8-12. The polarization of the

incident plane wave was here parallel to the xy plane. However, computations with perpendicular polarization showed similar results. The near field is composed of the incident and scattered light, where the former is assigned unit amplitude. The field inside a circumscribed circle with a radius of r_{csc}, equaling the maximum radius of the spheroid, cannot be calculated for theoretical reasons [38] and was set to zero. The position of the particle is indicated by an arrow in each graph (Figures 8-12) and the scale on the x- and y-axis is expressed in terms of rcsc. Note that the scale on the z-axis, showing the intensity of the near field, is the same in all graphs except in Figure 8, where the near field of the sphere is shown. The near field of the sphere reveals a significantly higher peak intensity than do any of the oblate or prolate spheroids. All particles were found to cause a standing wave pattern, resulting from interference between the incident and scattered fields, which has a highly forward directed component. The height and location of the peak of these near-field components depend on the shape and size (versus the wavelength) of the scattering object. The sphere (Figure 8 induces the highest near-field peak slightly shifted in the positive x direction. The oblate and weakly prolate shaped spheroids (Figures 9 and 10) have peaks of similar heights, but the location of the peak for the oblate spheroid is almost immediately behind the scattering particle, whereas the peak of the prolate is again slightly shifted in the positive x direction. Figures 11 and 12 show that the peak is clearly reduced when the prolate spheroid is elongated, leaving a slowly declining plateau.

The extension of the near field was evaluated in terms of a near-field radius, indicating where the maximum intensity had been reduced to 2.5 times that of the incident light. Values between 2.0 r_{csc} (for Prolate III at 940 nm) and 24.5 (for the sphere at 632.8 nm) were obtained. All values are presented in Table 2, both in terms of the radius of a circumscribed circle and of absolute values (12.1 μm for the oblate at 632.8 nm to 69.1 μm for the sphere at 632.8 nm). No significant difference in the near-field radius was obtained for incident light with parallel or perpendicular polarization. Furthermore, scattered light by an oblate spheroid was at both wavelengths shown to yield a significantly shorter near-field radius than a sphere. Also the elongation of the prolate spheroid was shown to reduce the near-field radius.

In contrast to the angular distribution of the far field, the near-field radius, used to evaluate the near field, is dependent on the light absorption in the spheroid. As it was not possible to evaluate the absorption of light using the programs with extended precision, the analysis of the influence of absorption similar to that of a red blood cell, had to be performed using programs with double precision limited to spheroids with moderate axial ratios. The near-field radius was decreased by on average 0.6 r_{csc} for prolate spheroids and 0.2 r_{csc} for oblate spheroids, all with an axial ratio close to unity, when the light absorption was incorporated in the T-matrix computations.

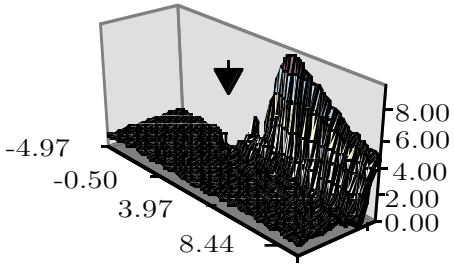

Figure 8: The near fields are shown, computed at 940 nm with a parallel polarization of the incident light, surrounding the five spheroids depicted in Figures 2 and 3. The incident plane wave propagates in the positive x direction and the intensity of the near field is given in relative units in the equatorial plane of the scattering object. An arrow indicates the position of the spheroid and the scale of the x- and y-axis is expressed in terms of the major axis of the spheroid, r_{csc}. The near field of the sphere is shown in this figure.

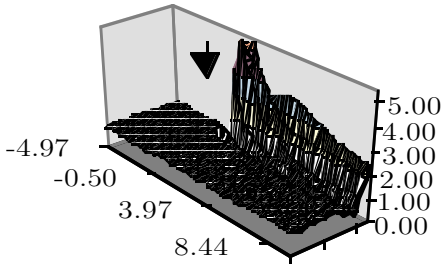

Figure 9: Same as Figure 8 but for the oblate spheroid shown in Figures 2 and 3.

5 Discussion

Computations on light propagation in blood are often performed in order to be able to correlate the results with those obtained from measurements [28, 31, 32]. Detailed information on biochemical and morphological properties of blood which are important to determine, both in vivo and in vitro [5, 6, 8, 13, 25, 32, 35], can be deduced and followed by relating measured to theoretical parameters. The choice of theoretical model and approximations must thus be made in close relation to physical reality. Measurements have proven that Mie theory can successfully be applied, when studying the size of randomly oriented red blood cells in a suspension [32]. The various shapes of the red blood cells are more difficult to examine, although several experimental studies [4, 19, 27] have measured the influence of cell shape and alignment on optical parameters. Multiple scattering models for a homogeneous medium with random distribution of scatterers, as well as Mie theory, assuming spherical scattering objects, may therefore be inappropriate for theoretical analysis of light transport in flowing blood. Instead we have here introduced the T-matrix

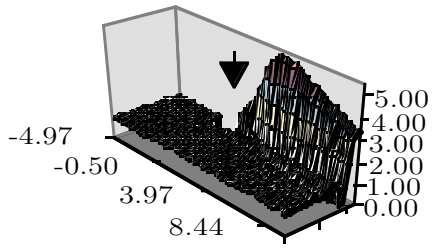

Figure 10: Same as Figure 8 but for the prolate spheroid I shown in Figures 2 and 3

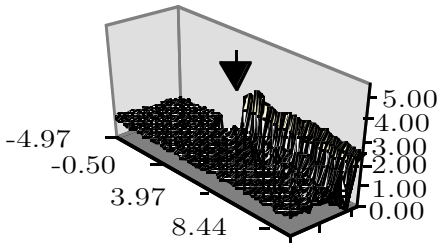

Figure 11: Same as Figure 8 but for the prolate spheroid II shown in Figures 2 and 3

formalism for spheroidal objects [3, 38] in the field of tissue optics. The T-matrix method is considered to be one of the most accurate and powerful techniques to compute light scattering by non-spherical particles, with sizes in the range of the wavelength. The computations in this study were performed for RBC volume equivalent, homogeneous spheroids.

Thus, we did not incorporate a cell membrane in the model, as it has been shown to have only a minor influence on the angular scattering pattern [17, 21]. The biconcave shape of a normal RBC under low or no shear stress was also neglected, though we acknowledge that the characteristic dips do perhaps influence the angular distribution of the scattered light. However, the general trend of the cell shape is unquestionably oblate shaped by nature. Moreover, healthy cells are flexible to facilitate their migration through thin capillaries and it is therefore reasonable to assume an average cell shape of a spheroid for red blood cells, when under moderate or high shear stress, or when affected by fluid dynamic interactions with surrounding cells [34].

Independent of how the far field was analyzed, the results imply a substantial impact of the cell shape on the light scattering. There are essentially three morphological properties, which here theoretically have been shown to characteristically affect the angular distribution of the scattered light. The general three dimensional

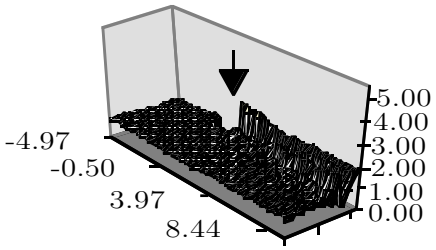

Figure 12: Same as Figure 8 but for the prolate spheroid III shown in Figures 2 and 3

	Oblate 632.8 nm		Sphere 632.8 nm		Oblate 940 nm		Sphere 940 nm		Prolate I 940 nm		Prolate II 940 nm		Prolate III 940 nm	
Polarization	∥	⊥	∥	⊥	∥	⊥	∥	⊥	∥	⊥	∥	⊥	∥	⊥
r_{nf} (no. r_{csc})	3.1	4.0	24.5	24.5	9.2	9.3	20.4	20.4	15.8	15.8	9.7	9.7	2.0	2.0
r_{nf} (μm)	12.1	15.6	69.1	69.1	36.0	36.4	57.5	57.5	61.8	61.8	52.4	52.4	13.0	13.0

Table 2: The near-field radius, r_{nf}, for the volume equivalents of a RBC was evaluated as the distance from the center of the particle to where the maximum intensity of the total field had decreased to 2.5 times that of the incident field. The results are shown both as absolute values in μm and relative a radius of a circumscribed circle of the particle (r_{csc}=maximum(a, b)).

shape of the scattering object, as well as the thickness of the particle along the direction of the incident light (here called the optical thickness), seem to have a manifest effect on the forward scattering component. Moreover, the back scattering component is highly influenced by the shape of the particle surface facing the incident light. The latter is clearly exemplified when varying the zenith incident angle of the oblate spheroid, shown in Figures 4 a-c. A significantly greater back scattering is obtained, when the light is impinging on a surface segment perpendicular to the direction of the incident light (Figures 4 a and c), compared to that for oblique incidence (Figure 4 b). Furthermore, the change in back scattering is less pronounced when the change in shape does not seriously affect the curvature of the surface, as for elongation of the prolate spheroids shown in Figure 5. The behavior of the forward scattering is completely different. The general trend here is an increase in intensity, when the direction of the incident light approaches that of the minor axis, irrespective of whether it is an oblate or prolate spheroid (see Figures 4, 6, 7 and Table 1). The forward scattering component thus tends, as previously mentioned, to be influenced by the thickness of the spheroid apparent to the incident light. For example, the oblate spheroid has a rather small optical thickness at incident angles of 0° and 45° and consequently a large forward scattering, as shown in Figures 4 and 6. In contrast, at an incident angle of 90°, meaning an incident beam along the major axis, yields a large optical thickness and thus reduced forward scattering. Furthermore, the optical thickness at an incident angle of 90° is even larger than for a volume equivalent sphere. Consequently, the scattering probability in the forward direction of the oblate spheroid at this incident angle is lower than that obtained for the sphere, as can be seen in Figure 6. This phenomenon is further exemplified in Figure 7 (940 nm). However, the optical thickness is not the

only parameter affecting the forward scattering. There seems to be a dominating influence of the three-dimensional shape, observed when keeping the zenith incident angle θ_i constant at 90° and instead changing the elongation. Despite the decrease in optical thickness apparent to the incident light perpendicular to the symmetry axis, a decrease in the forward scattering is observed in Figures 5 and 7 with more pronounced elongation. The three-dimensional shape of the spheroid has apparently a greater impact on the forward scattering for the prolate spheroid than the optical thickness, which indicates the complex nature of the scattered light.

Neither the angular distributions of scattered light nor the scattering probabilities (Figures 4-7) agree very well with the probability function of Henyey-Greenstein [9], which is the most frequently used probability function, when modeling light propagation in tissue. The Henyey-Greenstein function exhibits a clearly weaker forward scattering ($\theta_s = 1 - 15°$) and a larger side- and back scattering, than any of the theoretical results obtained in this study. It has previously been shown that the Henyey-Greenstein function describes the angular distribution of the scattering from dense tissue (skin) [12] with a g-factor of 0.82 well, but this has not been proven for whole blood with a substantially larger g-factor and is thus still an open question. The discrepancy may also indicate an averaging of several scattering events being incorporated in the Henyey-Greenstein function, i.e. it embodies multiple scattering rather than single scattering in view of electromagnetic theory.

All results from the far-field computations were obtained for both directions of the polarization. The polarization was in general shown to have a minor or insignificant influence on the distribution of scattered light, probably due to a relative refractive index close to unity [1]. In contrast, the wavelength of the incident light was shown to be a more important parameter. The distribution of scattered light is determined by the size of the scattering object relative to the wavelength, rather than the absolute value of the size. This can be seen in Table 1, which presents the results of far-field computations performed at two different wavelengths, 632.8 nm and 940 nm, i.e. two important wavelengths from an experimental point of view, which enables comparisons to be undertaken between experimental results and the theoretical calculations.

With these general observations in mind, it is interesting to model and analyze the impact of two authentic phenomena on the scattering pattern, i.e. sphering and elongation of blood. Sphering of an RBC volume equivalent oblate spheroid, results in lower and broader forward scattering (Figures 4 and 6) at incident angles of $\theta_i = 0°$ and 45°. This is in accordance with the previously mentioned general observations. The g-factor is a convenient parameter to describe the angular distribution of the scattering, when dealing with multiple scattering and it is therefore frequently used and measured within tissue optics. Experimental results obtained in an earlier study [26] revealed a small but distinct decrease in the g-factor of blood measured at 632.8 nm in combination with slow heating, when the disc shaped cells turned spherical due to the increase in temperature. The slightly lower average value of the g-factor for the sphere compared to the oblate spheroid (at both wavelengths), exhibited by the theoretical results obtained in this study (Table 1), is thus in accordance with the experimental results. However, the results presented here indicate that the g-factor

is only slightly changed with sphering (Table 1), though the angular distributions show major alterations. This indicates that a small change in a g-factor close to unity, can still correspond to a significant change in the angular distribution of the scattered light caused by cell shape transformations. Substantial information concerning changes in cell shape is thus lost when analyzing the light scattering in terms of the g-factor. The g-factor seems to be more influenced by changes and differences in cell size [27, 32].

The results obtained from the T-matrix computations have shown that the influence of shape, elongation and orientation of RBCs on the transport of light in blood in motion can be analyzed theoretically. According to Bitbol [4], the cells are randomly oriented and oblate shaped at low shear stress. The random orientation suggests that the average value of the g-factor for the three different incident angles (0°, 45° and 90°), i.e. 0.993 for the wavelength 940 nm, should be used. At intermediate shear stress, the cells have been shown to align themselves side-on, with the symmetry axis perpendicular to the flow direction. For many optical measurements of flowing blood, the probe light often passes the sample perpendicular to the flow direction, i.e. with an incident angle of approximately 90° from the symmetry axis of the cell (0° from the major axis). From Table 1 it is clear that this alignment would cause a decrease in the g-factor from 0.993 to 0.989 at 940 nm, i.e. a distribution of scattered light less forwardly directed. At even higher shear stress the cells become elongated, which according to Table 1 would again cause a slight decrease in the g-factor at an incident angle of 90°. Increasing the flow of blood would therefore cause a decrease in the forward scattering. The computed decrease in g-factor with increasing flow and shear stress corresponds well with experimental results obtained by Tomita et al. [35], Bitbol [4] and Lindberg et al. [19] on flowing blood. Cell orientation and elongation are therefore, together with the previous suggestion of re-suspension of aggregated cells [19, 35], also possible explanations of the decrease in light transmission and increase in reflection, with increasing shear rate.

When comparing experimental and theoretical results, we assume that the measurements were performed on blood, where the cells can be regarded as independent scatterers. The results of single scattering computations, based on for example the T-matrix formalism or Lorentz-Mie theory, can only under this assumption be valid when extrapolated to suspensions containing several scattering particles. This assumption is reasonable for diluted blood, often used for optical measurements in vitro. However, it has so far been unclear whether this approach can be employed to describe light scattering from whole blood, with an inter-particle distance estimated to approximately three times the RBC radius (center to center). By comparing the far field originating from a single sphere, or spheroid on the one hand and from bispheres, or clusters of spheroids on the other, Mishchenko et al. [23] and Vargas et al. [37] have shown that for a center-to-center inter-particle distance of more than four times the maximum radius, yields independent scattering, when the axial ratios of the scattering objects are unity, or close to unity, and the size of the particles is small. However, it is difficult to draw any firm conclusions concerning the light scattering by highly asymmetric, large RBCs from their results. We have therefore evaluated the near-field radius for light interaction with a single spheroid scatterer.

In the following we have considered the radius at which the intensity of the near field has decreased to 2.5 times that of the incident field. When the distance between the cells is in this range, or larger, we have assumed that the scattering by each cell can be considered as being independent. The results shown in Figures 8-12 and Table 2 suggest that the extension of the near field is strongly dependent on the shape of the scattering spheroid, as well as on the size, relative to the wavelength. The smallest near-field radius was 2.0 r_{csc} (13.0 μm for Prolate III) and the largest near-field radius, 24.5 r_{csc}, was obtained for the sphere evaluated at 632.8 nm, i.e. all spheroids were surrounded by near fields with significant extensions. Moreover, incorporating the absorption properties of the haemoglobin suspension inside the red blood cells in our spheroidal model, seems to have only a minor effect on the extension of the near field. It is thus clear that red blood cells in whole blood cannot be regarded as independent scatterers, in contrast to those in diluted blood. This might partly explain the larger impact, of the sphering on the g-factor found experimentally, on whole blood [26], compared to the theoretical results obtained in this work assuming independent scattering. It indicates that the concentration of RBCs must be considered when performing optical measurements on blood and that results obtained from measurements on diluted blood cannot simply be extrapolated to the in vivo case with whole blood.

6 Conclusions

A theoretical scattering model, taking the shape of the red blood cells into account, should be employed to better understand physiological phenomena concerning the shape of red blood cells from optical measurements. Only then can fundamental haematological and morphological properties of RBCs be optically extracted with sufficient accuracy. Applying the common Lorentz-Mie theory for blood in motion, i.e. assuming spherical red blood cells, seems inappropriate in the light of the results obtained in this study. The T-matrix method with extended precision was employed here, revealing that both alignment of RBC volume equivalent spheroids, sphering, and elongation have a significant influence on the angular distribution of the scattered light. The shape of the particle surface facing the incident light seems to have a large impact on the back scattered light, while the total, three-dimensional shape and the optical thickness apparent to the incident light, appear to mainly influence the forward scattering component. From these results it follows that the flow of the blood and the measurement geometry must be taken into account when analyzing optical measurements of blood.

The analysis of near fields surrounding the RBC volume equivalents, suggests that an inter-particle distance (center to surface of neighboring spheroid) larger than 3-24.5 times the maximum radius of the spheroid is required to be able to consider the RBCs as independent scatterers. The extension of the near field was shown to be dependent on the shape and size of the spheroid and wavelength used. In all, this implies that results obtained from optical measurements performed on diluted blood cannot simply be extrapolated to describe light scattering by whole

blood.

Acknowledgments

We wish to express our sincere gratitude to Jörgen Carlsson, who let us share his powerful computer. This work was financially supported by the Swedish Research Council for Engineering Sciences and Swedish Natural Science Foundation.

References

[1] S. Asano. Light scattering properties of spheroidal particles. *Appl. Opt.*, **18**, 712–723, 1979.

[2] P. W. Barber and S. C. Hill. *Light scattering by particles: computational methods.* World Scientific Publishing Co. Pte. Ltd. Singapore, 1990.

[3] P. W. Barber and C. Yeh. Scattering of electromagnetic waves by arbitrarily shaped dielectric bodies. *Appl. Opt.*, **14**, 2864–2872, 1975.

[4] M. Bitbol. Red blood cell orientation in orbit c = 0. *Biophys. J.*, **49**, 1055–1068, 1986.

[5] B. Chance, H. Liu, T. Kitai, , and Y. Zhang. Effects of solutes on optical properties of biological materials: models, cells, and tissues. *Anal. Biochem.*, **227**, 351–362, 1995.

[6] M. Cope and D. T. Delpy. System for long-term measurement of cerebral blood and tissue oxygenation on newborn infants by near infra-red transillumination. *Med. Biol. Eng. Comput.*, **26**, 289–294, 1988.

[7] E. Evans and Y.-C. Fung. Improved measurements of the erythrocyte geometry. *Microvasc. Res.*, **4**, 335–347, 1972.

[8] H. Hahn, A. Roggan, D. Schädel, U. Stock, H. Bäumler, , and F. Wondrazek. Die optischen eigenschaften von dicken schichten zirkulierenden humanblutes. *Minimal Invasive Medizin*, **7**, 79–90, 1996.

[9] L. G. Henyey and J. L. Greenstein. Diffuse radiation in the galaxy. *Astrophysics Journal*, **93**, 70–83, 1941.

[10] S. C. Hill, A. C. Hill, and P. W. Barber. Light scattering by size/shape distributions of soil particles and spheroids. *Appl. Opt.*, **23**, 1025–1031, 1984.

[11] A. Ishimaru. *Electromagnetic wave propagation, radiation, and scattering.* Prentice-Hall, Inc. New Jersey, 1991.

[12] S. L. Jacques, C. A. Alter, and S. A. Prahl. Angular dependence of hene laser light scattering by human dermis. *Lasers Life Sci.*, **1**, 309–333, 1987.

[13] F. F. Jöbsis. Noninvasive, infrared monitoring of cerebral and myocardial oxygen sufficiency and circulatory parameters. *Science*, **198**, 1264–1267, 1977.

[14] S. Kashima, A. Sohda, Y. Yagyu, and T. Ohsawa. Determination of deformability of erythrocytes by change in scattering cross section. *Jpn. J. Appl. Phys.*, **34**, 680–682, 1995.

[15] A. Kienle, M. S. Patterson, L. Ott, and R. Steiner. Determination of the scattering coefficient and the anisotropy factor from laser doppler spectra of liquids including blood. *Appl. Opt.*, **35**, 3404–3412, 1996.

[16] P. Latimer, D. M. Moore, and F. D. Bryant. Changes in total light scattering and absorption caused by changes in particle conformation. *J. Theoret. Biol.*, **21**, 348–367, 1968.

[17] P. Latimer and B. E. Pyle. Light scattering at various angles. theoretical predictions of the effects of particle volume changes. *Biophys. J.*, **12**, 764–773, 1972.

[18] J. C. Lin and A. W. Guy. A note on the optical scattering characteristics of whole blood. *IEEE Trans. Biomed. Eng.*, **21**, 43–45, 1974.

[19] L.-G. Lindberg and P.Å. Öberg. Optical properties of blood in motion. *Opt. Eng.*, **32**, 253–257, 1993.

[20] Y. Mendelson, A. C. Clermont, R. A. Peura, and B.-C. Lin. Blood glucose measurement by multiple attenuated total reflection and infrared absorption spectroscopy. *IEEE Trans. Biomed. Eng.*, **37**, 458–465, 1990.

[21] R. A. Meyer. Light scattering from red blood cell ghosts: sensitivity of angular dependent structure to membrane thickness and refractive index. *Appl. Opt.*, **16**, 2036–2038, 1977.

[22] M. I. Mishchenko. Light scattering by size-shape distributions of randomly oriented axially symmetric particles of a size comparable to a wavelength. *Appl. Opt.*, **34**, 4652–4666, 1993.

[23] M. I. Mishchenko, D. W. Mackowski, and L. D. Travis. Scattering of light by bispheres with touching and separated components. *Appl. Opt.*, **34**, 4589–4599, 1995.

[24] M. I. Mishchenko and L. D. Travis. T-matrix computations of light scattering by large spheroidal particles. *Opt. Comm.*, **109**, 16–21, 1994.

[25] N. Mohandas, Y. R. Kim, D. H. Tycko, J. Orlik, J. Wyatt, and W. Groner. Accurate and independent measurement of volume and hemoglobin concentration of individual red cells by laser light scattering. *Blood*, **68**, 506–513, 1986.

[26] A. M. K. Nilsson, G. W. Lucassen, W. Verkruysse, S. Andersson-Engels, and M. J. C. van Gemert. Changes in optical properties of human whole blood in vitro due to slow heating. *Photochem. Photobiol.*, **65**, 366–373, 1997.

[27] A. M. K. Nilsson, C. Sturesson, D. L. Liu, and S. Andersson-Engels. Changes in optical properties in conjunction with laser-induced thermotherapy. *Appl. Opt. (in press)*, 1997.

[28] L. Reynolds, C. Johnson, and A. Ishimaru. Diffuse reflectance from a finite blood medium: applications to the modeling of fiber optic catheters. *Appl. Opt.*, **15**, 2059–2067, 1976.

[29] A. Q. Sierra and A. V. D. Mora. Size-shape determination of nonspherical particles in suspension by means of full and depolarized static light scattering. *Appl. Opt.*, **34**, 6256–6262, 1995.

[30] J. M. Steinke and A. P. Shepherd. Reflectance measurements of hematocrit and oxyhemoglobin saturation. *Am. J. Physiol.*, **253**, H147–H153, 1987.

[31] J. M. Steinke and A. P. Shepherd. Comparison of mie theory and the light scattering of red blood cells. *Appl. Opt.*, **27**, 4027–4033, 1988.

[32] J. M. Steinke and A. P. Shepherd. Diffusion model of the optical absorbance of whole blood. *J. Opt. Soc. Am. A*, **5**, 813–822, 1988.

[33] G. J. Streekstra, A. G. Hoekstra, E.-J. Nijhof, and R. M. Heethaar. Light scattering by red blood cells in ektacytometry: Fraunhofer versus anomalous diffraction. *Appl. Opt.*, **32**, 2266–2272, 1993.

[34] M. Sugihara. Motion and deformation of a red blood cell in a shear flow: a two-dimensional simulation of the wall effect. *Biorheology*, **22**, 1–19, 1985.

[35] M. Tomita, M. Gotoh, M. Yamamoto, N. Tanahashi, and M. Kobari. Effects of hemolysis, hematocrit, rbc swelling, and flow rate on light scattering by blood in a 0.26 cm id transparent tube. *Biorheology*, **20**, 485–494, 1984.

[36] H. C. van de Hulst. *Light scattering by small particles.* Wiley, New York, 1957.

[37] W. E. Vargas, L. Cruz, L. F. Fonseca, and M. Gomez. T-matrix approach for calculating local fields around clusters of rotated spheroids. *Appl. Opt.*, **32**, 2164–2169, 1993.

[38] P. C. Waterman. Symmetry, unitarity and geometry in electromagnetic scattering. *Physical Review D*, **3**, 825–839, 1971.